



A Fully Coupled Numerical Model for Unbonded Post-tensioned Timber Structures

A. Ersin Dinçer¹ · Abdullah Demir²

Received: 18 May 2023 / Accepted: 26 March 2024
© The Author(s) 2024

Abstract

The paper presents a fully Lagrangian mesh-free solver to simulate the dynamic behavior of post-tensioned timber structures. Weakly Compressible Smoothed Particle Hydrodynamics (SPH) is employed to model both the timber and the tendon. An efficient and simple coupling method between the timber and the tendon is proposed by considering the numerical stability. Besides, the same coupling algorithm is used to model the interaction between column and beam elements. Although the column is treated as rigid in the simulations, the coupling algorithm accounts for the initial compression of the column resulting from post-tensioning. For the verification of the code for solids and material nonlinearity of timber, benchmark problems available in the literature are used. Finally, the solver's capability is demonstrated through dynamic analysis of post-tensioned timber structures. The solutions obtained for all the cases are in good agreement with the experimental and theoretical data, which indicates the applicability and accuracy of the solver.

1 Introduction

In historical construction practices, timber was employed as a rudimentary material, often as logs supporting roofs or functioning as two-force members in large-span timber structures (Crocetti 2016). Contemporary engineering practices have shifted towards the utilization of advanced timber elements such as laminated timber (Fleming and Ramage 2020), reinforced timber (Dietsch and Brandner 2015), post-strengthened (retrofitted) timber (Schober and Rautenstrauch 2007), prestressed timber (De Luca and Marano 2012), and post-tensioned timber elements (Wanninger and Frangi 2014; Mei et al. 2023). Researchers have shown their interest in timber by exploring various techniques and engineered timber made materials. Glulam, which is laminated timber, has been used for over a century and has been extensively used in engineering applications. Large shell structures have been built for many years, and reinforced structures have

also been developed. Timber-concrete composite constructions have been in use since the 1930s. Additionally, prestressed timber beams have been extensively researched and developed over the years.

Among these areas, post-tensioning in timber structures is a relatively recent concept, relying on enhancing the moment-carrying capacity of timber frame systems. In its basic application (Wanninger and Frangi 2014, 2016), post-tensioning involves the introduction of an unbonded tendon without additional structural elements. Energy dissipative elements, such as yielding steel angles (Di Cesare et al. 2019; Shu et al. 2019) and epoxied steels (Newcombe et al. 2008; Smith et al. 2014; Pampanin 2018) may be incorporated based on serviceability requirements at beam-column and column-foundation connections.

Unbonded post-tensioning represents a technique employed to enhance the load-bearing capacity of structural members and systems. In this method, a tendon is strategically placed within a hole, either drilled or left as a void within the geometry of the member. Following the jacking operation of the tendon, internal stresses manifest within the element, predominantly in compression, contingent upon the orientation of the tendon through the element's geometry. Consequently, the element acquires increased strength to resist bending forces, constituting the primary advantage of tensioning. Furthermore, the load-bearing capacity of joints is improved. In the study

✉ Abdullah Demir
abdullah.demir@agu.edu.tr

A. Ersin Dinçer
ersin.dincer@agu.edu.tr

¹ Department of Civil Engineering, Hydraulics Laboratory, Abdullah Gül University, Kayseri 38080, Turkey

² Department of Civil Engineering, Structural Laboratory, Abdullah Gül University, Kayseri 38080, Turkey

conducted by Mei et al. (2023), a notable finding underscores that augmenting prestress levels and the number of wires can effectively enhance joint bearing capacity. This implies that post-tensioning applications contribute not only to the moment-carrying capacity of the frame itself but also to the capacity of its joints. Such applications can be implemented either internally, as demonstrated by Wanninger and Frangi (2014), or externally, as indicated by Mei et al. (2023).

All the benefits associated with post-tensioning are applicable to the utilization of wooden members. Additionally, a rocking mechanism occurs at the beam-column connection, effectively mitigating the drawbacks inherent in rigid connections. As mentioned earlier, certain energy dissipative elements can be incorporated into the connections of post-tensioned timber structures. Importantly, these elements do not compromise the integrity of the rocking mechanism. Consequently, rocking motion is observed in all post-tensioned timber structures. In contrast, the phenomenon of rocking motion is not observed in structures made of concrete and their corresponding post-tensioned applications. Therefore, this study specifically focuses on the investigation of unbonded post-tensioned applications in timber structures, where the rocking mechanism is present.

The rocking mechanism denotes the rigid body oscillations of a freestanding structure on a surface. Despite its apparent simplicity, this phenomenon encompasses numerous complex dynamic phenomena, including impacts, sliding, and geometric and material nonlinearities, which vary depending on the specific problem (Chatzis and Smyth 2012a). Housner (1963) was the first to address this phenomenon, presenting a closed-form solution. Housner's closed-form solution has been applied, rederived for new conditions, or adapted in various research studies (Haroun and Ellaithy 1985; Zhang and Makris 2001; Prieto et al. 2004). From a finite element perspective, rocking motion consists of a contact problem. A specialized finite element method was proposed by Chatzis and Smyth (2012a, b) for rocking structures on deformable surfaces, and a conventional discrete finite element method was utilized to analyze a rocking podium on a shake table (Vassiliou et al. 2021). However, none of these methods devised for rocking motion have been employed in addressing post-tensioned timber problems. Instead, a team of researchers opted to utilize engineering standards (NZS 3101:1995) to achieve moment-rotation responses (Newcombe et al. 2008; Smith et al. 2014; Pamparin 2018), and employed ANSYS to determine the cyclic behavior of energy dissipative angles (Smith et al. 2014). Some researchers favored using OpenSees (Shu et al. 2019), while others preferred analytical methods (Wanninger and Frangi 2014, 2016; Fleming and Ramage 2020). Notably, in these analyses, tendons were modeled as path-defined forces rather than structural elements.

Adopting a more comprehensive method for analyzing post-tensioned timber structures is deemed more suitable, a necessity underscored by the complex nature of the problem, as highlighted in the research of Chatzis and Smyth (2012a). Specifically, the complexity arises from the presence of two distinct timber elements, namely the beam and column, each potentially possessing different moduli along their contact surface. To address this complexity, a finite model incorporating contact mechanics becomes essential, facilitating the generation of a self-generating contact surface without reliance on assumptions. This approach is crucial as it allows for the computation of internal stresses, a capability not inherent in a general rocking mechanism analysis. In addition to the timber model, a dedicated model for the tendon is imperative. Even if the tendon is bonded throughout its geometry, the potential for contact with the timber exists depending on the applied load or displacement. Utilizing a geometrically nonlinear model for the tendon proves instrumental in resolving this issue, ensuring a more accurate representation of the interaction dynamics between the tendon and timber elements.

In addition to the inherent complexity of the problem, predominantly characterized by geometric nonlinearities, the material aspect introduces an additional layer of intricacy. Wood, as an anisotropic material, exhibits mechanical properties contingent upon grain direction. Moreover, as a natural element, wood manifests various types with properties spanning a wide spectrum, influenced by grain orientation, growth patterns, geographical location, tree age, temperature, and moisture content (Gharib et al. 2017). Consequently, the material properties of wood and structures constructed from wood have become a focal point for researchers. Addressing the varied nature of wood, researchers have delved into the development of numerous nonlinear material models to replicate the intricate behavior of timber accurately (Oudjene and Khelifa 2009; Khennane et al. 2014; Sandhaas et al. 2020; Eslami et al. 2021; Rahman et al. 2022). In addition, the variety of material properties of wood originates a research area for selection of the correct wood and wood product (Lissouck et al. 2018; Özşahin et al. 2019; Schietzold et al. 2021; Gomez-Ceballos et al. 2022) for specialized form of structural elements. In this research area, multi-criteria decision methods, having a wide range of application area (Messaoudi et al. 2019; Demir and Dinçer 2023; Dinçer et al. 2023, 2024), are used for selection considering properties of woods.

Accordingly, in the present study, Smoothed Particle Hydrodynamics (SPH), initially proposed by Gingold and Monaghan (1977), is chosen as the modeling method to capture the rocking mechanism in post-tensioned timber structures. While SPH was originally introduced for astrophysical problems and then fluid dynamics, its application has extended across various disciplines. Numerous SPH models

have been developed for fluids (Demir et al. 2019, 2021; Dinçer et al. 2019; Demir 2020; Dinçer 2020; Demir and Dinçer 2023), solids (Gray et al. 2001; Antoci et al. 2007), and soils (Nonoyama et al. 2015; Niroumand et al. 2017). As a meshless method, SPH is particularly well-suited for modeling domains characterized by large displacements and rigid body motions. Capitalizing on this attribute, the authors previously proposed an SPH model for cables (Dinçer and Demir 2020), a system characterized by substantial displacement and rigid body motion. In the context of the present study, the SPH method is deemed suitable for modeling post-tensioning in timber structures due to its ability to address various nonlinearities. These include geometric nonlinearities arising from rigid body motion (rocking motion), geometric nonlinearities associated with the beam and tendon, and material nonlinearity stemming from the properties of timber materials.

In essence, the simulation of post-tensioned timber models is a challenging task, particularly when considering nonlinearities. A comprehensive simulation requires accurate modeling of both the tendon and timber elements. In prior numerical models, mesh-based methods were commonly favored, often neglecting the nonlinearity inherent in the tendon. As previously discussed, one of the primary advantages of SPH lies in its capacity to handle systems with substantial displacements, making it a preferable choice for tendon simulations. Moreover, coupling the tendon with the beam is a straightforward process for numerous numerical or even analytical models, provided the nonlinearity of the tendon hole in the beam is disregarded. However, when nonlinearities are considered, implementing a coupling algorithm becomes necessary, which can be intricate for many numerical methods. This study introduces an efficient coupling algorithm for tendon and timber elements by adapting the Shifting Surface of Solid Domain (SSOSD) developed for Fluid–Structure Interaction (FSI) problems by the authors. To the best of the authors' knowledge, this study represents the first attempt at utilizing SPH to model unbonded post-tensioned timber structures. Furthermore, the tendon's geometric nonlinearity is considered for the first time. Accordingly, for two-dimensional simulations, a one-way coupling algorithm is proposed, wherein the influence of beam elements throughout the tendon is considered. In contrast, the effect of tendon elements on the beam is solely accounted for at the caps of the beam. Consequently, the geometric uniformity of the beam in two dimensions is preserved.

The structure of the paper unfolds as follows: Initially, the formulation and equations of SPH employed for simulating timber and tendon elements are expounded upon, and the coupling algorithm is introduced. Subsequently, the paper proceeds to a validation case, demonstrating the prowess of the SPH solid solver. It is worth noting that validations on

tendon simulations can be referenced in the research of Dinçer and Demir (2020). Additionally, the nonlinear material model is tested for its effectiveness. Finally, the paper delves into the simulation of unbonded post-tensioned timber elements, showcasing the solver's capabilities in this specific context.

2 Methodology

2.1 Equations for an elastic body

The governing equations of continuum mechanics include the continuity, momentum, and energy equations. The continuity equation for a compressible body reads

$$\frac{d\rho}{dt} = -\rho \nabla \cdot v \quad (1)$$

where ρ is the density and v is the velocity vector. Similarly, the momentum equation can be shown as

$$\frac{dv}{dt} = \frac{1}{\rho} \nabla \cdot \sigma + g \quad (2)$$

where d/dt denotes the derivative following the motion, σ denotes the Cauchy stress tensor, and g is the gravitational acceleration vector. The stress tensor includes direction-dependent and independent stresses represented as

$$\sigma^{ij} = -P\delta^{ij} + \tau^{ij} \quad (3)$$

where i and j are the Cartesian components in x and y directions, P is the pressure, τ^{ij} is the deviatoric stress. In fluid mechanics, the stress is proportional to strain rate whereas in solid mechanics, the stress is the function of strain and strain rate.

If the displacements are small, the stress rate is proportional to strain rate through shear modulus, μ . The rate of change of τ^{ij} is then given by Gray et al. (2001).

$$\frac{d\tau^{ij}}{dt} = 2\mu \left(\dot{\epsilon}^{ij} - \frac{1}{3} \delta^{ij} \dot{\epsilon}^{kk} \right) + \tau^{ik} \Omega^{jk} + \Omega^{ik} \tau^{kj} \quad (4)$$

where

$$\dot{\epsilon}^{ij} = \frac{1}{2} \left(\frac{\partial v^i}{\partial x^j} + \frac{\partial v^j}{\partial x^i} \right) \quad (5)$$

$$\Omega^{ij} = \frac{1}{2} \left(\frac{\partial v^i}{\partial x^j} - \frac{\partial v^j}{\partial x^i} \right) \quad (6)$$

$\dot{\epsilon}^{ij}$ is the transformation tensor and Ω^{ij} is the rotation tensor.

The pressure–volume behavior for an elastic body can be computed from the equation of state, which is appropriate for small variations of density.

$$P = \frac{K}{\rho_0} (\rho - \rho_0) \tag{7}$$

where ρ_0 is the reference density and K is the bulk modulus.

2.2 Material model

Wood, characterized as an anisotropic material, exhibits varying properties depending on its type. Additionally, composite wood-made structural elements, such as glued laminated timbers (glulam), contribute to the diversity of engineered materials. Numerous approaches have been proposed to capture the stress–strain relationship of timber and timber-made engineered materials (Oudjene and Khelifa 2009; Khennane et al. 2014; Valipour et al. 2014; Karagiannis et al. 2016, 2017; Gharib et al. 2017; Sandhaas et al. 2020; Eslami et al. 2021; Rahman et al. 2022). However, it is important to note that this study adopts a linearly elastic, perfectly plastic material behavior for timber, as illustrated in Fig. 1. This specific behavior, previously employed for glued laminated timber arches (Zhou et al. 2020), serves as the basis for the analysis in this study.

In Fig. 1, f_c and f_t are compression and tension strength, respectively. Corresponding strains in compression and tension are ϵ_{cy} and ϵ_t , respectively.

2.3 The SPH formulations

The SPH representation of continuity and momentum equations for particle a reads

$$\frac{d\rho_a}{dt} = \sum_b m_b v_{ab} \cdot \nabla_a W_{ab} \tag{8}$$

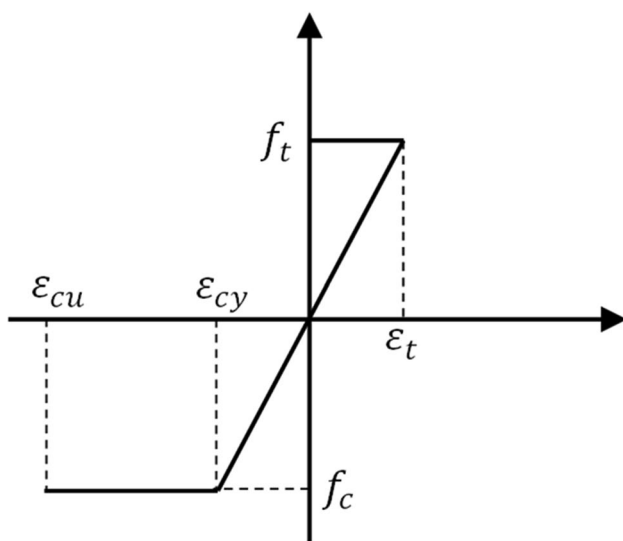


Fig. 1 Stress–strain relationship of glulam timber

$$\frac{dv_a^i}{dt} = \sum_b m_b \left(\frac{\sigma_a^{ij}}{\rho_a^2} + \frac{\sigma_b^{ij}}{\rho_b^2} + \Pi_{ab} \delta^{ij} + R_{ab}^{ij} f^n - \frac{\omega}{A} C_{ab} \right) \frac{\partial W_{ab}}{\partial x_a^j} + g^i + \frac{s_s^i}{m_a^i} + \frac{s_t^i}{m_a^i} \tag{9}$$

where the summation is over all particles b around a , m_b is mass of the particle b . The kernel W_{ab} is a function of the distance between the particles a and b , and ∇_a denotes the gradient taken with respect to the coordinates of particle a . In the present study, Wendland C2 kernel with a support domain of $2h$ is used where h is the smoothing length of kernel. The forces coming from the interaction between two bodies are shown with s_s^i and s_t^i representing the force on the solid body and on the tendon, respectively. A detailed discussion about interaction forces can be found in part 2.4.

In the momentum equation the last three terms in the brackets have been introduced to prevent numerical problems due to SPH algorithm. The term Π_{ab} produces a shear and bulk viscosity. It is called artificial viscosity in SPH and shown as:

$$\Pi_{ab} = \frac{-\phi \left(\frac{h(v_a - v_b) \cdot (r_a - r_b)}{|r_a - r_b|^2 + 0.001h^2} \right) 0.5(c_a - c_b)}{0.5(\rho_a + \rho_b)} \tag{10}$$

where c is the speed of sound, r is the position vector of a particle and ϕ is the problem dependent parameter explained in research of Gray et al. (2001) and Antoci et al. (2007).

To remove the tensile instability, a control term, $R_{ab}^{ij} f^n$, called artificial stress is added to the momentum equation,

$$f_{ab} = \frac{W(r_{ab})}{W(\Delta p)} \tag{11}$$

$$R_{ab}^{ij} = R_a^{ij} + R_b^{ij} \tag{12}$$

where Δp is the particle spacing. Note that if $R^{ij} < 0$ the artificial stress has the same sign as a positive pressure term and acts to keep the particles apart. A detailed explanation about the derivation of the terms in artificial stress equation can be found in the research of Gray et al. (2001).

2.4 Equations of the tendon

The tendon is a specialized form of elastic body with distinctive characteristics. It is presumed that the tendon exhibits solely unidirectional strain due to its specific geometry. Therefore, in the local coordinate system, ϵ^{ij} has only unidirectional strain. The term, $\frac{\omega}{A} C_{ab}$, shown in the momentum equation is exclusively utilized when the material is tendon. This utilization was introduced by the authors to mitigate unnecessary oscillations identified in SPH analysis of tendons (Dinçer and Demir 2020). In this term, A is the unstretched cross-sectional area of the tendon and ω is a

constant representing the rate of the damping, C_{ab} for each direction can be shown as:

$$C_{ab} = \frac{m_a V_a}{\rho_a^2} + \frac{m_b V_b}{\rho_b^2} \tag{13}$$

2.5 Interactions of domains

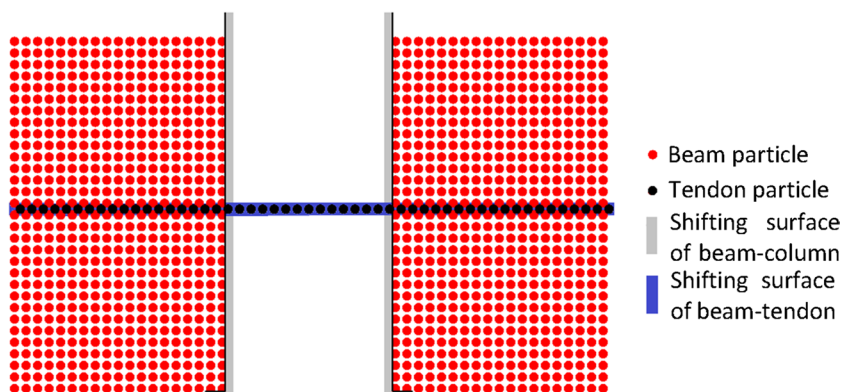
Systematic particle size reduction is employed to achieve convergence (mesh independence) in a solid domain. However, when dealing with a contact between two solid domains, achieving convergence becomes more challenging due to the constraint imposed by the contact line, which the neighboring domain must not violate. Consequently, the number of particles at the contact surface may need to be increased to delineate a line between adjacent particles. Failure to do so may result in a semi-rigid connection at the contact. To address such challenges, the authors proposed a method specifically designed for these problems, Shifting the Surface of Structural Domain (SSOSD) (Dinçer et al. 2019). Originally introduced for fluid–structure interaction, this method is adapted for structure–structure interaction in the current study context. Instead of allowing a particle to penetrate the neighboring domain, the surface of the neighboring domain is shifted to the opposite surface. This is a crucial step, especially in contrast to finite element methods, where neighboring domains can be modeled very close to each other. Consequently, an intermediate domain is generated through this shifting surface approach. If a particle exists within this intermediate domain, it is removed based on a predefined nonlinear function. This removal process occurs gradually over multiple time steps, allowing particles to suspend in the intermediate domain. The nonlinear function dictates that the more overlap between SPH particles, the more they are subjected to displacements proportional to their overlap, and vice versa. The equation is given below.

$$({}_{new}O^{(i-1)})_n = (O^{(i-1)})_n - d + e^{-\left(\frac{|(O^{(i-1)})_n|}{|d|}\right)} d \tag{14}$$

where $(O^{(i-1)})_n$ is the overlap in local normal direction n of boundary surface, $({}_{new}O^{(i-1)})_n$ is the new assumed overlap (which is the amount of displacement to be applied), d is a problem dependent vector in local normal direction n . This parameter, d , defines the depth of the boundary violation. In the context of unbonded post-tensioned timber problems, selecting this crucial parameter is undertaken to ensure that the analytically calculated initial compression of the column is attained during the initial stage of SPH simulations. Furthermore, the depth of the shifting surface is chosen to be identical to the initial particle spacing, aiming to fulfill the initial contact condition, as illustrated in Fig. 2. The forces acting on the boundary particles of the beam are computed by evaluating their overlap using a suitable Lagrange multiplier. Subsequently, these forces are incorporated into the momentum equation as an external force, represented by the term, s_s^i .

Any displacement of the beam and column particles induces a change in the configuration of the tendon hole. Particularly, the geometry of the hole exhibits nonlinear characteristics under higher deformations of the beam. To incorporate this geometric nonlinearity, the interaction between the tendon (depicted in black particles in Fig. 2) and the boundary particles of the beam is composed throughout the hole. In this regard, initially overlapping contact lines, visualized as a continuous blue region in Fig. 3(b), are utilized in the simulations of the tendon element. These contact lines, obtained from the boundary particles, serve as a representation of the tendon hole's geometry. The coordinates of these contact lines are derived from the coordinates of the existing beam particles corresponding to the tendon hole. Subsequently, the internal forces within the tendon are computed using the SSOSD method. A shifted surface is defined on both sides of the hole, and the value of the shifting surface is set equal to the tendon radius, which is initially the same as the hole radius. This ensures that the contact lines

Fig. 2 SPH illustration of tendon elements, beam elements and column representing SSOSD lines



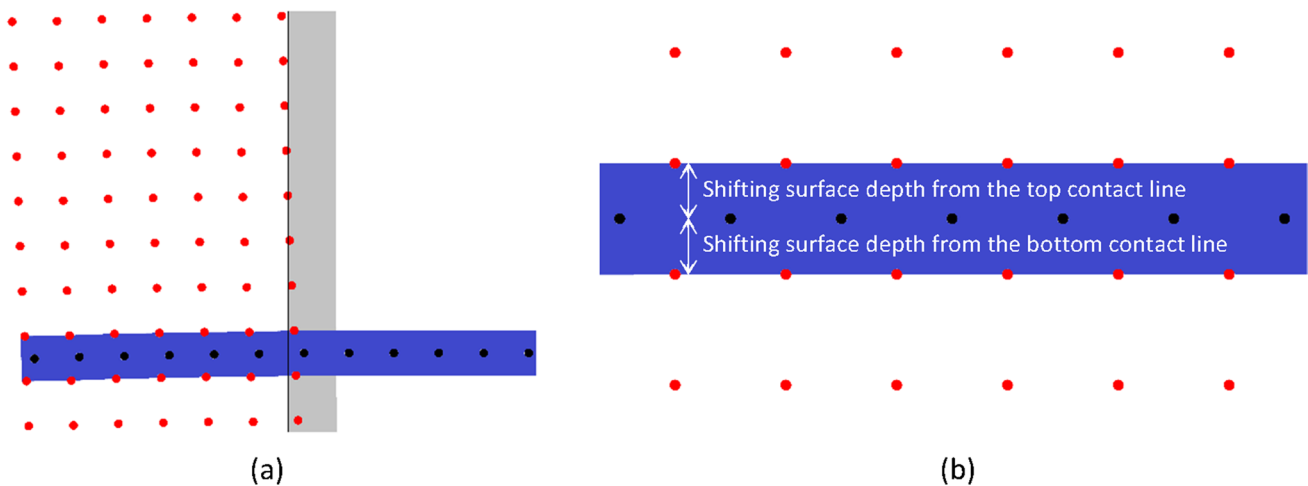


Fig. 3 Detailed view of (a) beam column interaction and (b) tendon beam interaction

overlap for the initial condition. Therefore, the influence of the tendon on the beam is mediated through the geometry of the defined hole, constituting a reciprocal interaction. The force exerted on the beam due to the presence of the tendon is integrated into the momentum equation with s_s^i term. Similarly, the forces on the tendon element due to its contact with the hole are represented by s_t^i term.

The application of the SSOSD method empowers the analyzer to attain a robust and smooth interaction. Notably, penetrations become more discernible with a reference contact line. In the context of the present study, analyzing penetrations through the contact line holds significant importance as it defines the neutral axis. As illustrated in Fig. 3(a), the neutral axis is distinctly defined with the utilization of the SSOSD method, providing a clear representation of the surface.

3 Results

3.1 Validations of solid model

To validate the accuracy of the solid component of the numerical model, a homogeneous beam clamped at both ends as employed by Khayyer et al. (2021), is utilized. Khayyer et al. (2021) predominantly focused on the analysis of composite elastic structures in their research, utilizing the Hamiltonian Smoothed Particle Hydrodynamics (HSPH) for the analysis. In their study, the beam experiences a uniform load applied throughout its geometry, as depicted in Fig. 4(a). The dimensions of the thin beam include a thickness of 0.012 m and a length of 0.2 m. The applied uniformly distributed load is 20 N/m. The material's modulus of elasticity is 2.4e7 Pa, Poisson's ratio is considered as zero, and the density is 1100 kg/m³. Both ends of the beam are

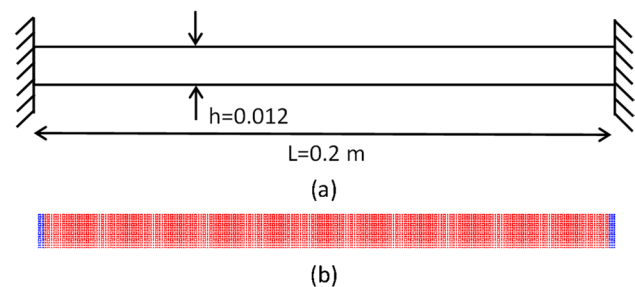


Fig. 4 (a) Geometry of beam and (b) SPH discretization of geometry

clamped, and Khayyer et al. (2021) addressed the boundary conditions of the fixed end support by fixing the boundary particles in space.

To overcome the potential issues associated with absolute fixing of boundary particles, where a particle's position is not revised and velocity is set to zero in each time step, the authors propose the use of an intermediate zone on the beam. Absolute fixing is applied to each loose end of these intermediate zones, allowing for more adaptable boundaries. This prevents discontinuities throughout the interface of SPH and boundary particles. The rigidity of the intermediate zone is set to be high but not infinite, and this can be achieved by adjusting the modulus of elasticity (rigidity) of the intermediate zone. The discretization of the intermediate zone is illustrated in Fig. 4(b).

For the convergence test, the particle size is systematically reduced from 1 mm to 0.5 mm. Convergence is deemed achieved for mid-span deflections when the particle spacing reaches 0.75 mm. The maximum allowable time step size is set at 8e-5 s. Results are then compared with the theoretical solution and prior findings by Khayyer et al. (2021). Both the results of the convergence tests and the comparison are presented in Fig. 5. Discrepancies between the theoretical

and numerical results originated from the boundary model of the proposed method. While the convergence results in the research of Khayyer et al. (2021) begin with higher mid-span deflections, the proposed model's convergence results start with lower deflections. In the proposed boundary condition, larger particle sizes lead to longer boundary regions. With the increase in the length of the boundary region, the midspan deflection naturally decreases. Additionally, internal stresses are comparatively illustrated in Fig. 6, revealing relatively higher stresses at both ends of the beam. This higher stress is attributed to the boundary method used in the present study. The presence of an intermediate zone at fixed ends leads to slightly higher stresses. Although these higher stresses result in lower mid-span deflections compared to those in the research of Khayyer et al. (2021) (see Fig. 5), convergence is achieved, and the calculated mid-span deflections closely align with the theoretical results.

3.2 Validation of material model

In the material model used in the present study, timber exhibits linear elastic behavior up to a defined limit. Beyond this elastic limit, its behavior is characterized as perfectly plastic for the compression part. The material model is applied to both directions of the grain. The adopted model

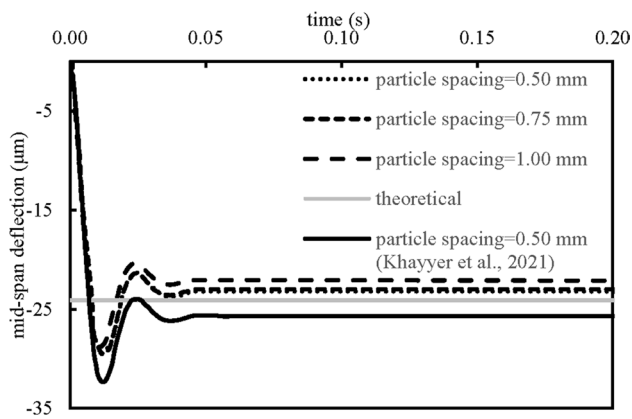
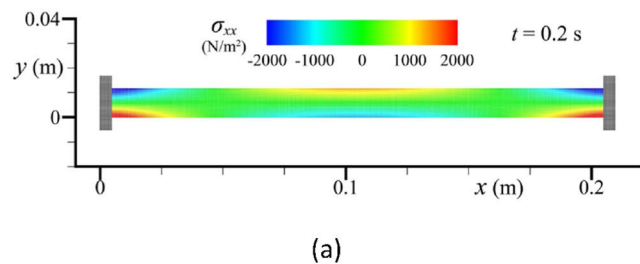


Fig. 5 Results of convergence test



is validated using experimental data reported in the research of Karagiannis et al. (2017) and employed in subsequent research (Karagiannis et al. 2016; Eslami et al. 2021; Rahman et al. 2022) as verification cases.

Two experiments are utilized as validation cases, one for compression and the other for tension. In both cases, the load is applied parallel to the grain direction of the timber, with specimen dimensions provided in Fig. 7. The average values for Young's modulus of the case samples are defined as 2050 MPa for compression and 10,949 MPa for tension, according to Karagiannis et al. (2017). Additionally, the strengths are taken as 33 MPa and 36.2 MPa, respectively. SPH analyses are conducted with a particle spacing of 0.5 mm. The comparison of the SPH solution and experimental results is presented in Fig. 8 and Fig. 9. It is important to note that the material models used in the reference studies differ from the one employed in this study. Consequently, some disparity in results is expected due to the use of non-identical material models. Nevertheless, the results of the reference studies using the same benchmark problem are depicted in Fig. 8 and Fig. 9 for comparison.

3.3 Post-tensioned timber frame

The numerical model is developed in two dimensions based on the series of experiments conducted by Wanninger and Frangi (2014, 2016). The cited articles were derived from the experiments, initially documented in a report on post-tensioned timber frame structures (Wanninger 2015). For this research, only the first series of experiments focusing on the connection of post-tensioned timber frames under gravity loads, is utilized. Notably, hand calculations were employed for analysis in the original research of Wanninger and Frangi (2014).

In the aforementioned study, an inventive post-tensioned joint was developed using glued laminated timber (GL24h) and ash hardwood (D40) with material properties sourced from the research of Porteous and Kermani (2013), as outlined in Table 1. Notably, the joint design excluded any additional steel elements, relying solely on the tendon positioned at the center of the frame. Instead of utilizing a steel shear

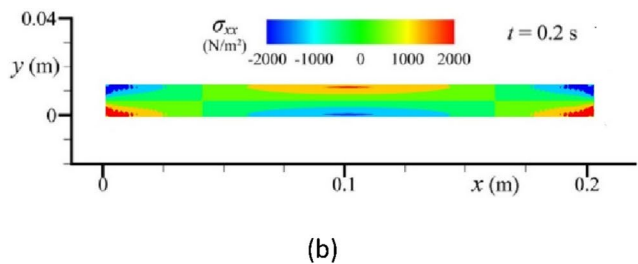


Fig. 6 Internal stresses of (a) Khayyer et al. (2021) and (b) proposed method

Fig. 7 Test specimens defined for compression (a) and tension (b)

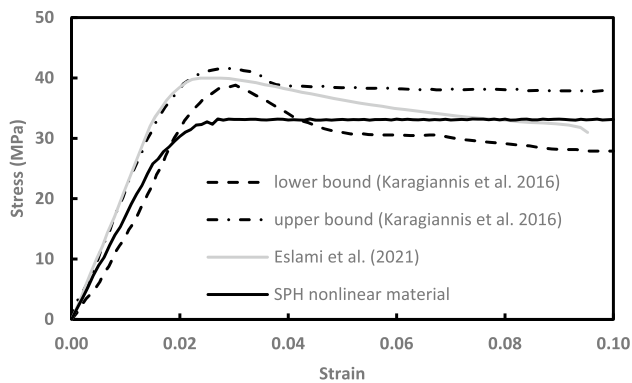
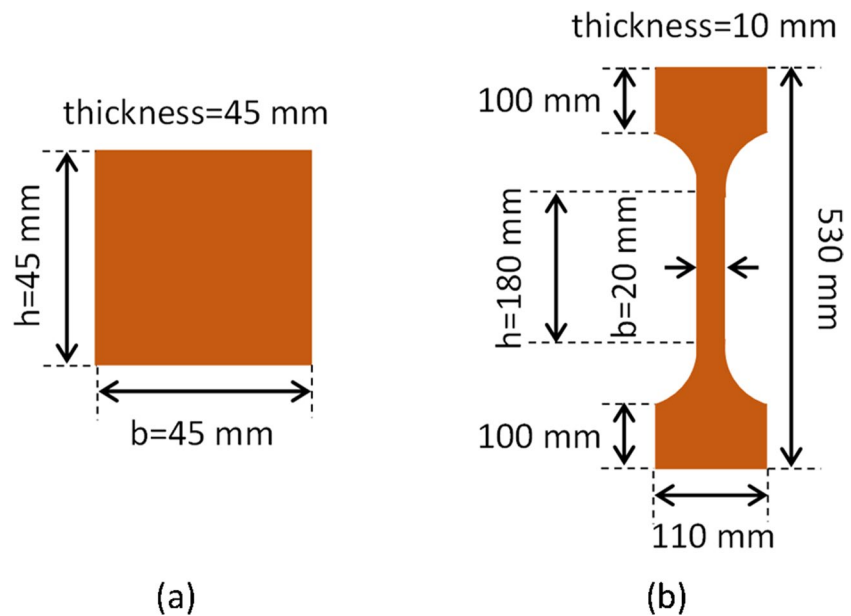


Fig. 8 Comparison between SPH and experimental results of compression test

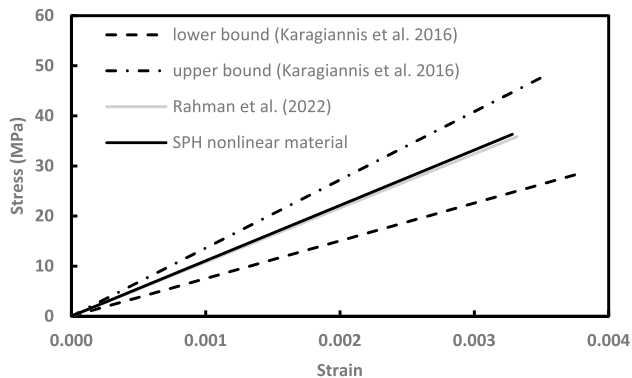


Fig. 9 Comparison between SHP and experimental results of tension test

key, hardwood was employed. Additionally, a 50 mm steel plate was placed at the end of the beam to ensure uniform transmission of the tendon load on the beam surface. The materials used and the experimental geometry are visually represented in Fig. 10, while further details about the measurement tools utilized in the experiment are available in the research of Wanninger and Frangi (2014).

In the experimental setup, two glulam timber frames were symmetrically positioned on either side of a column, primarily composed of hardwood. Notably, no additional materials were incorporated, aside from the post-tensioning tendon. Despite the applied tension on the tendon leading to an increase in shear force between the frame and the column, the frame was intentionally offset with a 4 cm indentation, serving as an effective shear key. As depicted in Fig. 10 and detailed in the research of Wanninger and Frangi (2014), a force was applied to the frame. The force history persisted for a duration of 1 h, encompassing both symmetric and unsymmetric loadings, with cyclic increases in load. In contrast, this study applies a uniform increase in load to the structure, with a loading rate of 250 N/s. While the defined rate does not significantly impact the results, it is acknowledged that this rate may induce oscillations at the initial stages of loading. Given the expectation that these oscillations will dampen early in the simulation, a higher loading rate is chosen to optimize computational efficiency.

The initial tension in the tendon, set at 550 kN, remains constant until the applied load reaches its limit, eventually increasing to almost 800 kN depending on the transverse applied load. In the research of Wanninger and Frangi (2014), experimental results were differentiated for tendon

elongation, a concept also applicable to the proposed analytical model. The model of Wanninger and Frangi (2014) draws inspiration from the static analysis of a rigid beam on an elastic foundation, resembling the Winkler type of foundation. In this analogy, the rigid beam corresponds to the contact face of the timber frame, and the elastic foundation corresponds to the contact face of the column. It is known that timber-made structural elements are designed with longitudinal grain directions. Therefore, the analogy was

defined in that research as a stiff beam and soft column considering the grain of column and beam. There are springs, capable only of resisting compression (see Fig. 11(b)), situated between these contact faces. The static calculation of rotation (θ), neutral axis (x), moment (M), change in tendon force (P), and maximum stress (σ_1) on the contact surface was determined statically for the corresponding applied load (Fig. 11(a)).

Table 1 Material properties

Material name	Young's modulus	Compression strength	Tension strength
Glued laminated timber (GL24h) (E_0)	11,000 MPa	22 MPa	19.2 MPa
Glued laminated timber (GL24h) (E_{90})	300 MPa	3 MPa	0.5 MPa
Hardwood made of ash (D40) (E_0)	13,000 MPa	26 MPa	24 MPa
Hardwood made of ash (D40) (E_{90})	860 MPa	8.3 MPa	0.6 MPa
Steel cap (S420)	200 GPa	420 MPa	420 MPa
Steel tendon (Y1770 4-06)	197 GPa	-	1770 MPa

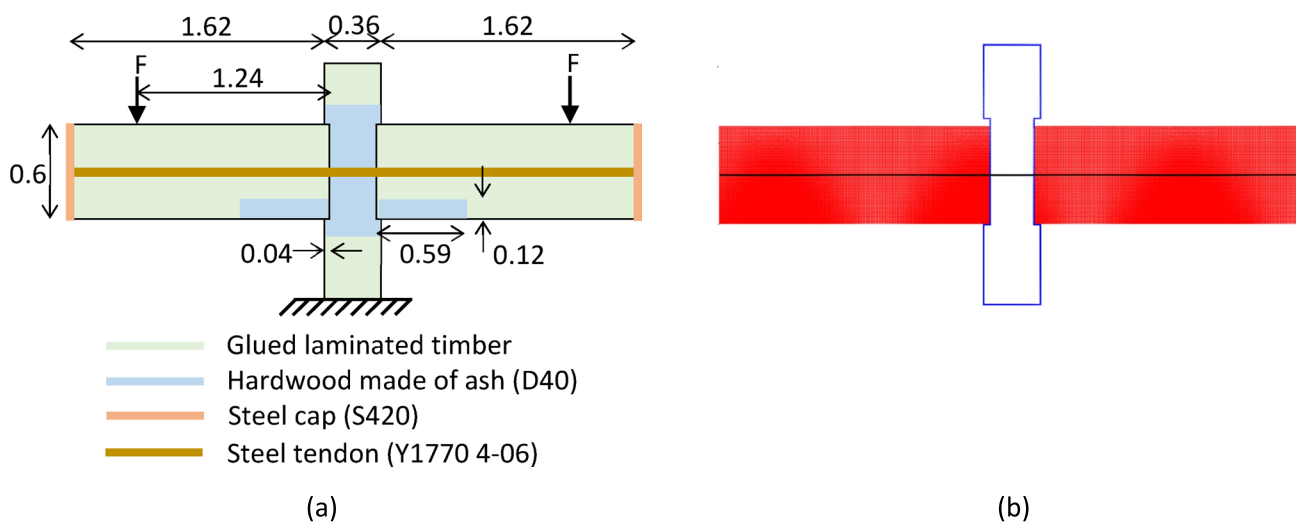


Fig. 10 (a) Materials and geometry of the experiment (in meters) and (b) particle representation of the experimental setup

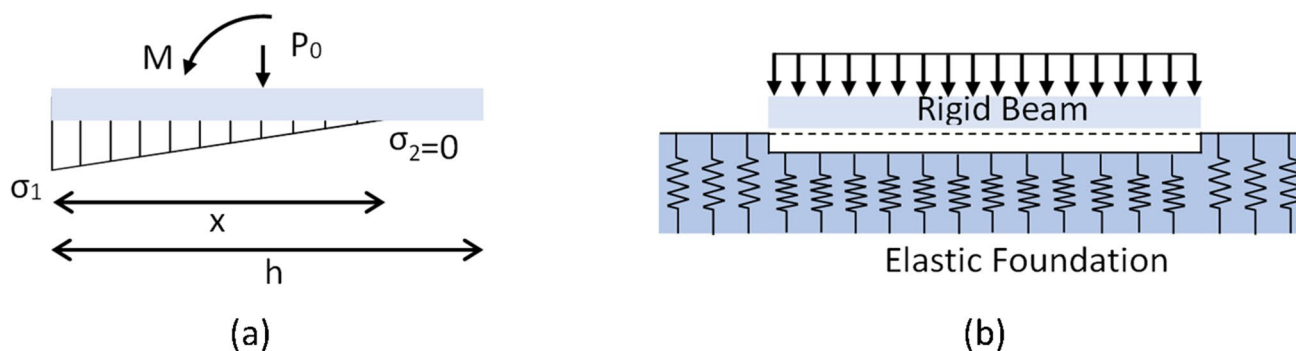


Fig. 11 (a) Free body diagram of the contact (b) inspired from beam on elastic foundation problem

In the simulations, the initial particle spacing for both beam and tendon elements is set at 1 cm. Consequently, 9960 particles are used to represent a single beam element, and 360 particles are allocated for the tendon. The maximum time limit is taken as $1.00\text{e-}4$ s. The Young's modulus of the beam is considered homogeneous throughout the geometry, with a value of 11,000 MPa. The SSOSD method is employed for both beam-column and beam-tendon interactions. The depth of the shifting surface is set as the initial particle spacing for beam-column interactions and half of the initial tendon particle spacing for beam-tendon interactions. As mentioned in the methodology part, a proper value of parameter, d , in the equation of SSOSD (Eq. (15)) is selected to satisfy the initial compression of the column due to the initial tendon stress. The initial compression is analytically calculated as 0.38 mm (Wanninger and Frangi 2014). In contrast, a higher value for parameter, d , is preferred to minimize the penetration depth of tendon.

4 Results and discussion

The tendon force, with a 4 cm indentation serving as a shear key, is the primary stabilizing factor. At the beginning of the experiment, the tendon force was raised to 550 kN. In numerical simulations, achieving a tendon force smaller than the initial value is not possible. However, in the experiments, the tendon force decreases during cyclic loading (refer to Fig. 12). This decrease is attributed to plastic deformations caused by local stresses on the timber surface. Numerically, an early increase in tendon force is observed (Fig. 12), resulting from oscillations that dampen out when the rotation angle, and consequently, the vertical deflection, is very low.

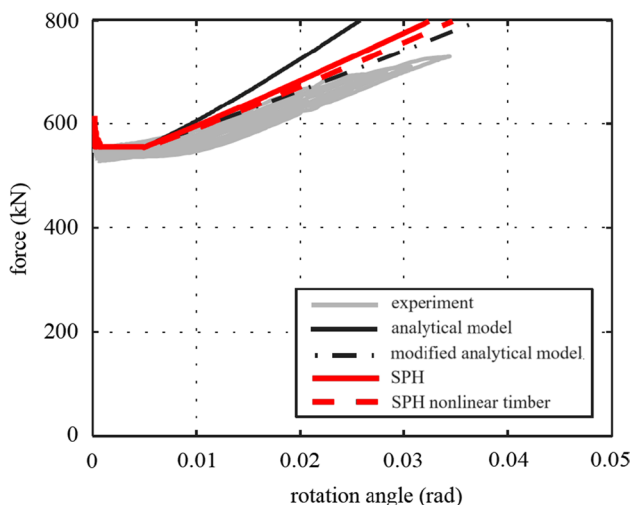


Fig. 12 Tendon force with respect to rotation angle

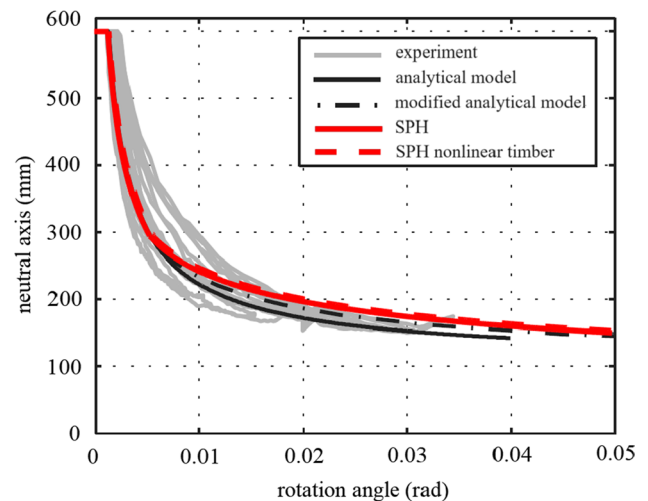


Fig. 13 Neutral axis with respect to rotation angle

Figure 13 illustrates the change in neutral axis depth with the rotation angle. At the initial stage of the loading where the rotation angle is low, the neutral axis depth remains constant and equal to the depth of the beam. As the rotation angle approaches approximately 0.0012 rad, the neutral axis starts to decrease. The numerical and analytical models predict consistent results up to a rotation angle of 0.008 rad. Beyond this threshold, the model predictions diverge. Although the predictions for neutral axis depth are close to each other and to the experimental data, notable differences are observed.

According to Wanninger and Frangi (2014), a potential reason for the variance between experimental and analytical results is the larger hole in the specimen compared to the tendon, allowing for tendon movement during experiments. In the modified analytical model of Wanninger and Frangi (2014), the spring constant derived from the rigid beam on an elastic foundation model was arbitrarily reduced when the maximum stress in the interface reaches 10 MPa. However, in the numerical model, there is no need for external intervention to capture timber behavior, as the geometric nonlinear behavior of the solid body and tendon is naturally considered. Moreover, the accuracy of the SPH model is enhanced by the inclusion of material nonlinearities.

The relationship between moment and rotation angle is illustrated in Fig. 14. In the experimental setup, the moment was computed by introducing a rotational spring, and it was directly calculated by multiplying the applied force with the distance between the load application point and the column-beam interface. Conversely, in the numerical model, the neutral axis and moment are derived from internal stresses at the beam-column interface, thereby considering the geometric nonlinear behavior of the beam element. It's noteworthy that the analytical model of Wanninger and Frangi (2014)

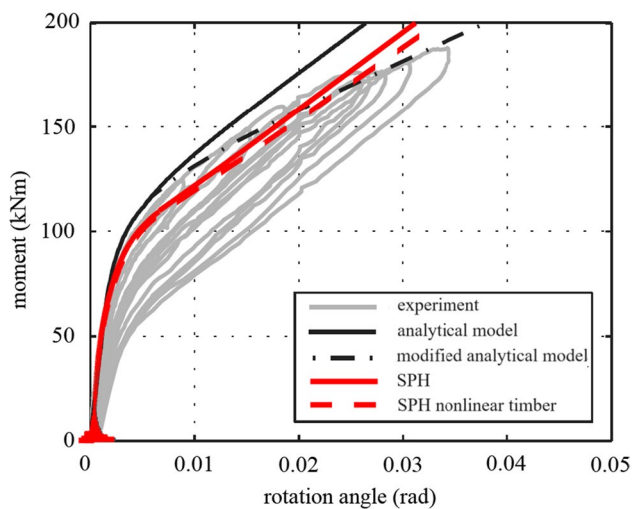


Fig. 14 Moment with respect to rotation angle

neglects the energy dissipated from the system. To investigate the impact of plastic deformations causing energy dissipation, a stress–strain relationship adopting linearly elastic perfectly plastic behavior is employed for timber materials modeled in SPH. Both linear and nonlinear material results are presented in the comparative figures. The disparity between SPH solutions with linear and nonlinear material behavior of timber directly indicates that the contact parts of the timber beam, composed of hardwood, yield. Stress concentration on hardwood (D40) leads to an increase in stress up to the plastic limit of hardwood with the rotation of the frame. Consequently, due to this plastic deformation, the rotation of the beam increases, as evident from Fig. 12 and Fig. 14. Nevertheless, there is a difference between experimental results and the predictions of the proposed model. The material behavior of timber is the main reason for the difference between the experiment and prediction of proposed model in which characteristic values for material properties (Table 1) are used.

Additionally, oscillations are observed at the initial stages of loading. The higher loading rate chosen in the numerical method, along with the initially applied tendon force, contributes to these early oscillations. Even a minor disturbance in the transverse direction of the tendon, induced by vertical loading, can result in elevated forces on the timber beam element from the tendon. Moreover, it is observed that the numerically predicted moment diverges from the analytical models sooner than anticipated. The earlier divergence is primarily attributed to nonlinear effects on both the beam and the tendon, arising from the geometry of the tendon hole considered in the numerical model.

The curve depicting the applied load and rotation angle for smaller rotation angles is derived from the load time history of the experiments in the research of Wanninger and

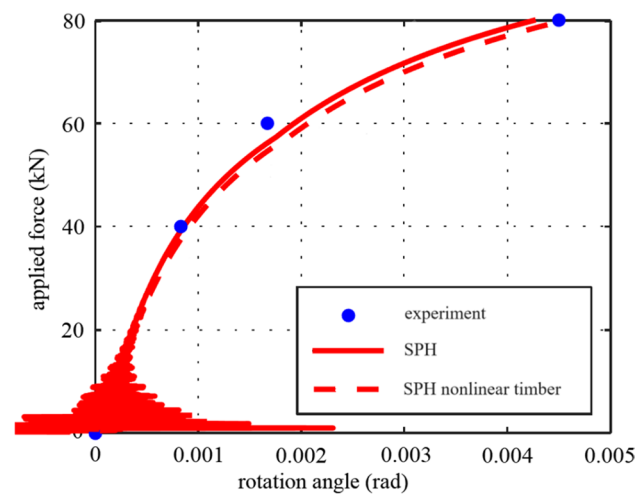


Fig. 15 Applied load with respect to rotation angle

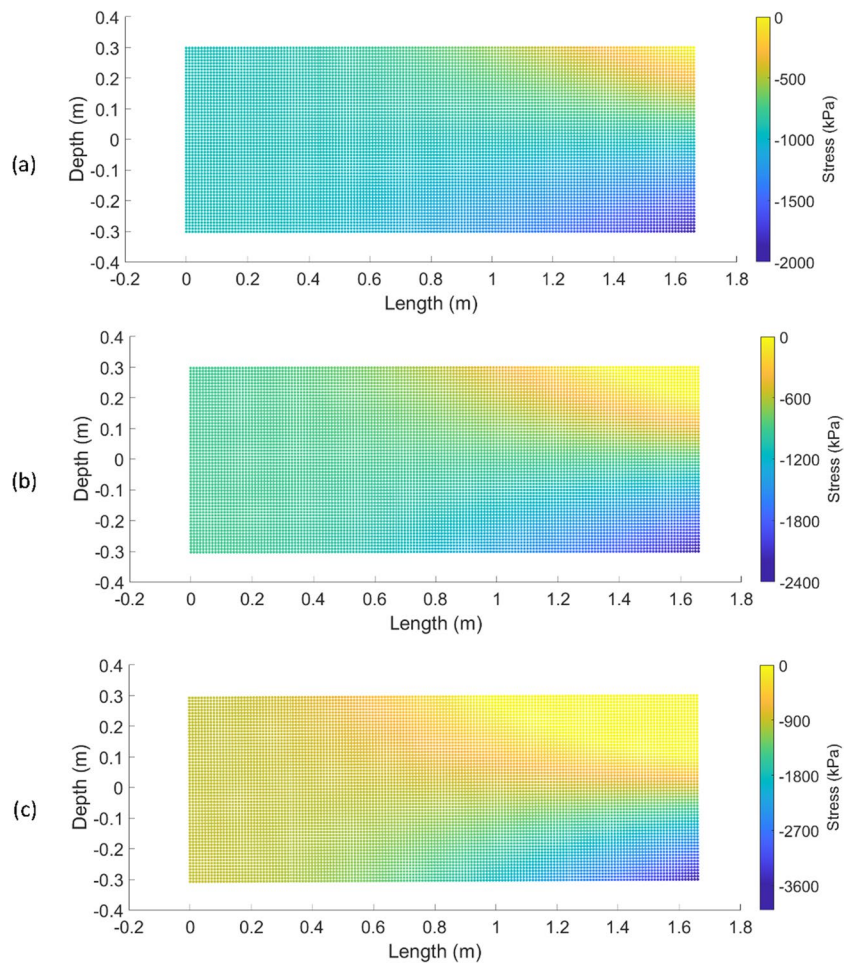
Frangi (2014). This reference data is represented as a scatter plot in Fig. 15. Initial oscillations are more remarkable in this figure, given that the rotation angles are very small compared to those in Fig. 12 and Fig. 14. Despite the evident initial oscillations, the numerical predictions of the applied load concerning rotation angles align closely with the experimental data. Consequently, it can be inferred that the initial oscillations do not significantly impact the simulation results in the later stages of loading.

Internal stress in the beam element was not depicted in the research of Wanninger and Frangi (2014). To address this gap, internal stress in the beam under specific loading conditions are illustrated in Fig. 16. These loading conditions are chosen for particular cases, where the applied force versus rotation angle is provided as scatter in Fig. 15. It is worth noting that an increase in the transverse load leads to rotation as seen in Fig. 15, which results in an opening in the column face of the beam due to inherent motion of rocking. In Fig. 16, longitudinal internal stress of the beam reveals a zero-stress region at the top right of the beam where the opening occurs between the beam and column.

5 Conclusion

A coupled SPH-based solver is introduced to effectively replicate the behavior of unbonded post-tensioned timber structures subjected to vertical loading. In this innovative approach, both the timber and tendon models are formulated within the SPH framework. A dedicated contact algorithm is devised to account for the geometric nonlinearities within the tendon hole in the timber. This identical contact algorithm is adeptly employed to emulate the interaction between beam and column elements. Additionally, a linearly elastic perfectly plastic material model is adopted for

Fig. 16 Internal stress in longitudinal direction for (a) 40kN, (b) 60kN and (c) 80kN transverse loads.



timber, facilitating the consideration of column compression resulting from the initial tendon stress. The outcomes of the numerical investigations in this study clearly demonstrate the efficacy of the proposed coupled SPH solver, coupled with the developed contact algorithm, in accurately capturing the intricate interactions between timber and tendon elements. To the best of the authors' knowledge, this is the first study presenting a fully coupled SPH solver to simulate post-tensioned timber frames.

The application of SPH in simulating the dynamic behavior of post-tensioned timber structures, as presented in this manuscript, brings forth both advantages and limitations. SPH proves advantageous in addressing geometric nonlinearities arising from rigid body motion, complex interactions between timber and tendon elements, and material nonlinearity due to the properties of timber materials. However, the inherent particle-based nature of SPH poses challenges in capturing certain mechanical effects, such as anisotropy resulting from the microstructure of cellular timber material, viscous behavior, and creep. The resolution limitations of the SPH method may hinder its ability to fully represent microstructural features

influencing anisotropic behavior. Additionally, while the model has been enhanced to predict internal stress distribution within timber elements, it is essential to acknowledge that SPH, as a meshless method, may face difficulties in providing detailed local behavior predictions compared to more established methods like FEM. Consequently, there is a need for further research to develop a more comprehensive material model for SPH, particularly considering the intricate characteristics of wood materials. Despite these challenges, the study introduces a novel methodology for analyzing wooden structures using SPH, opening up new research avenues in this field and showcasing the efficacy of the proposed coupled SPH solver in capturing the complex interactions within post-tensioned timber frames.

Authors' contributions Dr. Diñer and Dr. Demir make the same contribution for each part/step of the research.

Funding Open access funding provided by the Scientific and Technological Research Council of Türkiye (TÜBİTAK).

Data availability Not applicable.

Declarations

Ethical Approval Not applicable.

Competing Interests Not applicable.

Open Access This article is licensed under a Creative Commons Attribution 4.0 International License, which permits use, sharing, adaptation, distribution and reproduction in any medium or format, as long as you give appropriate credit to the original author(s) and the source, provide a link to the Creative Commons licence, and indicate if changes were made. The images or other third party material in this article are included in the article's Creative Commons licence, unless indicated otherwise in a credit line to the material. If material is not included in the article's Creative Commons licence and your intended use is not permitted by statutory regulation or exceeds the permitted use, you will need to obtain permission directly from the copyright holder. To view a copy of this licence, visit <http://creativecommons.org/licenses/by/4.0/>.

References

- Antoci C, Gallati M, Sibilla S (2007) Numerical simulation of fluid-structure interaction by SPH. *Comput Struct* 85:879–890. <https://doi.org/10.1016/j.compstruc.2007.01.002>
- Chatzis MN, Smyth AW (2012a) Robust Modeling of the Rocking Problem. *J Eng Mech* 138:247–262. [https://doi.org/10.1061/\(asce\)em.1943-7889.0000329](https://doi.org/10.1061/(asce)em.1943-7889.0000329)
- Chatzis MN, Smyth AW (2012b) Modeling of the 3D rocking problem. *Int J Non Linear Mech* 47:85–98. <https://doi.org/10.1016/j.ijnonlinmec.2012.02.004>
- Crocetti R (2016) Large-Span Timber Structures. *Proceedings of the World Congress on Civil, Structural, and Environmental Engineering* 1–23. <https://doi.org/10.11159/icseem16.124>
- De Luca V, Marano C (2012) Prestressed glulam timbers reinforced with steel bars. *Constr Build Mater* 30:206–217. <https://doi.org/10.1016/j.conbuildmat.2011.11.016>
- Demir A (2020) Hydro-elastic analysis of standing submerged structures under seismic excitations with sph-fem approach. *Latin American Journal of Solids and Structures* 17:1–14. <https://doi.org/10.1590/1679-78256266>
- Demir A, Dinçer AE, Bozkuş Z, Tijsseling AS (2019) Numerical and experimental investigation of damping in a dam-break problem with fluid-structure interaction. *J Zhejiang Univ, Sci, A* 20:258–271. <https://doi.org/10.1631/jzus.A1800520>
- Demir A, Dinçer AE, Öztürk Ş, Kazaz I (2021) Numerical and experimental investigation of sloshing in a water tank with a fully coupled fluid-structure interaction method. *Progress Computational Fluid Dynamics, Int J* 21:103–114
- Demir A, Dinçer AE (2023) Efficient disaster waste management: identifying suitable temporary sites using an emission-aware approach after the Kahramanmaraş earthquakes. *Int J Environ Sci Technol* 20:13143–13158
- Di Cesare A, Ponzio FC, Pampanin S et al (2019) Displacement based design of post-tensioned timber framed buildings with dissipative rocking mechanism. *Soil Dyn Earthq Eng* 116:317–330. <https://doi.org/10.1016/j.soildyn.2018.10.019>
- Dietsch P, Brandner R (2015) Self-tapping screws and threaded rods as reinforcement for structural timber elements-A state-of-the-art report. *Constr Build Mater* 97:78–89. <https://doi.org/10.1016/j.conbuildmat.2015.04.028>
- Dinçer AE, Demir A, Bozkuş Z, Tijsseling AS (2019) Fully Coupled Smoothed Particle Hydrodynamics-Finite Element Method Approach for Fluid-Structure Interaction Problems With Large Deflections. *J Fluids Eng, Transactions ASME* 141:1–13. <https://doi.org/10.1115/1.4043058>
- Dinçer AE, Demir A, Yılmaz K (2024) Multi-objective turbine allocation on a wind farm site. *Appl Energy* 355:122346. <https://doi.org/10.1016/j.apenergy.2023.122346>
- Dinçer AE, Demir A (2020) Application of smoothed particle hydrodynamics to structural cable analysis. *Appl Sci* 10(24):8983. <https://doi.org/10.3390/app10248983>
- Dinçer AE, Demir A, Yılmaz K (2023) Enhancing wind turbine site selection through a novel wake penalty criterion. *Energy* 129096
- Dinçer AE (2020) Experimental and numerical investigation of hyper-elastic submerged structures strengthened with cable under seismic excitations. *European Journal of Environmental and Civil Engineering* 1–20. <https://doi.org/10.1080/19648189.2020.1837253>
- Eslami H, Jayasinghe LB, Waldmann D (2021) Nonlinear three-dimensional anisotropic material model for failure analysis of timber. *Eng Fail Anal* 130:. <https://doi.org/10.1016/j.engfailanal.2021.105764>
- Fleming PH, Ramage MH (2020) Full-scale construction and testing of stress-laminated columns made with low-grade wood. *Constr Build Mater* 230:. <https://doi.org/10.1016/j.conbuildmat.2019.116952>
- Gharib M, Hassanieh A, Valipour H, Bradford MA (2017) Three-dimensional constitutive modelling of arbitrarily orientated timber based on continuum damage mechanics. *Finite Elem Anal Des* 135:79–90. <https://doi.org/10.1016/j.finel.2017.07.008>
- Gingold RA, Monaghan JJ (1977) Smoothed particle hydrodynamics: theory and application to non-spherical stars. *Mon Not R Astr Soc* 181:375–389
- Gomez-Ceballos WG, Gamboa-Marrufo M, Grondin F (2022) Multi-criteria assessment of a high-performance glulam through numerical simulation. *Eng Struct* 256:114021
- Gray JP, Monaghan JJ, Swift RP (2001) SPH elastic dynamics. *Comput Methods Appl Mech Engrg* 190:6641–6662
- Haroun MA, Ellaithy HM (1985) Model for Flexible Tanks Undergoing Rocking. *J Eng Mech* 111:143–157. [https://doi.org/10.1061/\(asce\)0733-9399\(1985\)111:2\(143\)](https://doi.org/10.1061/(asce)0733-9399(1985)111:2(143))
- Housner GW (1963) The behavior of inverted pendulum structures during earthquakes. *Bull Seismol Soc Am* 53:403–417
- Karagiannis V, Málaga-Chuquitaype C, Elghazouli AY (2016) Modified foundation modelling of dowel embedment in glulam connections. *Constr Build Mater* 102:1168–1179. <https://doi.org/10.1016/j.conbuildmat.2015.09.021>
- Karagiannis V, Málaga-Chuquitaype C, Elghazouli AY (2017) Behaviour of hybrid timber-steel beam-to-column connections. *Eng Struct* 131:243–263
- Khayyer A, Shimizu Y, Gotoh H, Nagashima K (2021) A coupled incompressible SPH-Hamiltonian SPH solver for hydroelastic FSI corresponding to composite structures. *Appl Math Model* 94:242–271. <https://doi.org/10.1016/j.apm.2021.01.011>
- Khennane A, Khelifa M, Bleron L, Viguier J (2014) Numerical modelling of ductile damage evolution in tensile and bending tests of timber structures. *Mech Mater* 68:228–236. <https://doi.org/10.1016/j.mechmat.2013.09.004>
- Lissouck RO, Pommier R, Taillandier F et al (2018) A decision support tool approach based on the Electre TRI-B method for the valorisation of tropical timbers from the Congo Basin: an application for glulam products. *Southern Forests: a J Forest Sci* 80:361–371
- Mei L, Wu M, Guo N et al (2023) Experimental and theoretical analyses on the mechanical properties of prestressed glulam continuous beam joints. *Eur J Wood Prod* 81:857–870. <https://doi.org/10.1007/s00107-022-01922-3>
- Messaoudi D, Settou N, Negrou B et al (2019) Site selection methodology for the wind-powered hydrogen refueling station based on AHP-GIS in Adrar, Algeria. *Energy Procedia* 162:67–76

- Newcombe MP, Pampanin S, Buchanan A, Palermo A (2008) Section analysis and cyclic behavior of post-tensioned jointed ductile connections for multi-story timber buildings. *J Earthquake Eng* 12:83–110. <https://doi.org/10.1080/13632460801925632>
- Niroumand H, Mehrizi MEM, Saaly M (2017) Application of SPH Method in Simulation of Failure of Soil and Rocks Exposed to Great Pressure. *Soil Mech Found Eng* 54:216–223. <https://doi.org/10.1007/s11204-017-9461-5>
- Nonoyama H, Moriguchi S, Sawada K, Yashima A (2015) Slope stability analysis using smoothed particle hydrodynamics (SPH) method. *Soils Found* 55:458–470. <https://doi.org/10.1016/j.sandf.2015.02.019>
- Oudjene M, Khelifa M (2009) Elasto-plastic constitutive law for wood behaviour under compressive loadings. *Constr Build Mater* 23:3359–3366. <https://doi.org/10.1016/j.conbuildmat.2009.06.034>
- Özşahin Ş, Singer H, Temiz A, Yıldırım İ (2019) Selection of softwood species for structural and non-structural timber construction by using the analytic hierarchy process (AHP) and the multiobjective optimization on the basis of ratio analysis (MOORA). *Balt For* 25(2):281–288
- Pampanin S (2018) Numerical and experimental investigation on low damage steel-timber post-tensioned beam-column. In: *Proc 16th European Conference on Earthquake Engineering*, pp 1–12
- Porteous J, Kermani A (2013) *Structural timber design to Eurocode 5*. John Wiley & Sons
- Prieto F, Lourenço PB, Oliveira CS (2004) Impulsive Dirac-delta forces in the rocking motion. *Earthq Eng Struct Dyn* 33:839–857. <https://doi.org/10.1002/eqe.381>
- Rahman SA, Ashraf M, Subhani M, Reiner J (2022) Comparison of continuum damage models for nonlinear finite element analysis of timber under tension in parallel and perpendicular to grain directions. *Eur J Wood Prod* 80:771–790. <https://doi.org/10.1007/s00107-022-01820-8>
- Sandhaas C, Sarnaghi AK, van de Kuilen JW (2020) Numerical modelling of timber and timber joints: computational aspects. *Wood Sci Technol* 54:31–61. <https://doi.org/10.1007/s00226-019-01142-8>
- Schietzold FN, Graf W, Kaliske M (2021) Multi-objective optimization of tree trunk axes in glulam beam design considering fuzzy probability-based random fields. *ASCE-ASME J Risk Uncertainty Eng Systems, Part b: Mechanical Eng* 7:020913
- Schober KU, Rautenstrauch K (2007) Post-strengthening of timber structures with CFRP's. *Materials Structures/materials Et Constructions* 40:27–35. <https://doi.org/10.1617/s11527-006-9128-6>
- Shu Z, Li Z, He M et al (2019) Seismic design and performance evaluation of self-centering timber moment resisting frames. *Soil Dyn Earthq Eng* 119:346–357. <https://doi.org/10.1016/j.soildyn.2018.08.038>
- Smith T, Ponzio FC, Di Cesare A et al (2014) Post-tensioned glulam beam-column joints with advanced damping systems: Testing and numerical analysis. *J Earthquake Eng* 18:147–167. <https://doi.org/10.1080/13632469.2013.835291>
- Valipour H, Khorsandnia N, Crews K, Foster S (2014) A simple strategy for constitutive modelling of timber. *Constr Build Mater* 53:138–148
- Vassiliou MF, Broccardo M, Cengiz C et al (2021) Shake table testing of a rocking podium: Results of a blind prediction contest. *Earthq Eng Struct Dyn* 50:1043–1062. <https://doi.org/10.1002/eqe.3386>
- Wanninger F (2015) Post-tensioned Timber Frame Structures. *IBK Bericht* 364. <https://doi.org/10.3929/ethz-a-010563008>
- Wanninger F, Frangi A (2014) Experimental and analytical analysis of a post-tensioned timber connection under gravity loads. *Eng Struct* 70:117–129. <https://doi.org/10.1016/j.engstruct.2014.03.042>
- Wanninger F, Frangi A (2016) Experimental and analytical analysis of a post-tensioned timber frame under horizontal loads. *Eng Struct* 113:16–25. <https://doi.org/10.1016/j.engstruct.2016.01.029>
- Zhang J, Makris N (2001) Rocking response of free-standing blocks under cycloidal pulses. *J Eng Mech* 127:473–483
- Zhou J, Li C, Ke L, et al (2020) Experimental Study on Loading Capacity of Glued-Laminated Timber Arches Subjected to Vertical Concentrated Loads. *Advances in Civil Engineering* 2020. <https://doi.org/10.1155/2020/7987414>

Publisher's Note Springer Nature remains neutral with regard to jurisdictional claims in published maps and institutional affiliations.